Angular Harmonic Hall Voltage and Magnetoresistance Measurements of Pt/FeCoB and Pt-Ti/FeCoB Bilayers for Spin Hall Conductivity Determination

Witold Skowroński, Krzysztof Grochot, Piotr Rzeszut, Stanisław Łazarski, Grzegorz Gajoch, Cezary Worek, Jarosław Kanak, Tomasz Stobiecki, Jürgen Langer, Berthold Ocker, *Member, IEEE*, and Mehran Vafaee

***Abstract*— Materials with significant spin-orbit coupling enable efficient spin-to-charge interconversion, which can be utilized in novel spin electronic devices. A number of elements, mainly heavy metals (HMs), have been identified to produce a sizable spin current (j_s), while supplied with a charge current (j), detected mainly in the neighboring ferromagnetic (FM) layer. Apart from the spin Hall angle $\theta_{SH} = j_s/j$, spin Hall conductivity (σ_{SH}) is an important parameter, which takes also the resistivity of the material into account. In this work, we present a measurement protocol of the HM/FM bilayers, which enables for a precise σ_{SH} determination. Static transport measurements, including resistivity and magnetization measurements, are accompanied by the angular harmonic Hall voltage analysis in a dedicated low-noise rotating probe station. Dynamic characterization includes effective magnetization and magnetization damping measurement, which enable HM/FM interface absorption calculation. We validate the measurement protocol in Pt and Pt-Ti underlayers in contact with FeCoB and present σ_{SH} of up to 3.3 $\times$ 10^5 S/m, which exceeds the values typically measured in other HM, such as W or Ta.**

***Index Terms*— Anisotropic magnetoresistance (AMR), ferromagnetic resonance (FMR), magnetic thin films, spin Hall effect, spin Hall magnetoresistance (SMR), spintronics.**

Manuscript received May 31, 2021; revised August 16, 2021 and September 30, 2021; accepted October 18, 2021. Date of publication November 2, 2021; date of current version December 1, 2021. The work of Krzysztof Grochot, Stanisław Łazarski, and Tomasz Stobiecki was supported by the National Science Centre, Poland, under Grant UMO-2016/23/B/ST3/01430. This work was supported by the National Science Centre, Poland, under Grant UMO-2015/17/D/ST3/00500. The review of this article was arranged by Editor L. Ge. *(Corresponding author: Witold Skowroński.)*

Witold Skowroński, Piotr Rzeszut, Stanisław Łazarski, Grzegorz Gajoch, Cezary Worek, and Jarosław Kanak are with the Institute of Electronics, AGH University of Science and Technology, 30-059 Kraków, Poland (e-mail: skowron@agh.edu.pl).

Krzysztof Grochot and Tomasz Stobiecki are with the Institute of Electronics, and the Faculty of Physics and Applied Computer Science, AGH University of Science and Technology, 30-059 Kraków, Poland.

Jürgen Langer, Berthold Ocker, and Mehran Vafaee are with Singulus Technologies AG, 63796 Kahl am Main, Germany (e-mail: mehran.khanjani@singulus.de).

Color versions of one or more figures in this article are available at https://doi.org/10.1109/TED.2021.3122999.

Digital Object Identifier 10.1109/TED.2021.3122999

I. Introduction

UTILIZING spin of the electron in addition to its charge opens up the way for the design of novel electronic devices [1]. The magnetic material, whose properties can be controlled using the spin current, is utilized widely in magnetic field sensors, data storage devices [2], radio-frequency (RF) electronics [3], and, more recently, in hardware implementation of biomimetic circuits [4]. It has been recently proposed that non-magnetic elements with high spin-orbit coupling can act as a source of the spin current [5]. In such spin-orbit torque (SOT) effect, the spin current (j_s) is generated as result of the charge current (j), with electron current, spin current, and spin vectors being orthogonal to each other [6]. Since its discovery, there have been multiple studies on SOT in different materials exhibiting spin-orbit coupling and the effect is now quantified using the so-called spin Hall angle (θ_{SH}) = j_s/j [7], [8]. Several methods of determination of θ_{SH} were proposed, such as ferromagnetic resonance (FMR) line-shape analysis [9], harmonic Hall voltage measurement [10], Kerr-effect-based optical determination [11], spin Hall magnetoresistance (SMR) [12], and threshold current magnetization switching [13]. All these methods require slightly different multilayer structure, or different ferromagnetic detecting layer's anisotropy axis and post-analysis, which enables quantitative investigation of material parameters.

In this article, we present an experimental protocol for the detailed measurement of spin Hall efficiency based on static and dynamic electrical measurements. We select a conventional system composed of a Pt/FeCoB bilayer together with a recently proposed [14] Pt-Ti/FeCoB system for the protocol verification. The presented protocol does not require special conditions, as opposed to perpendicular magnetic anisotropy of the FM for in-plane harmonic Hall voltage determination or negligible field-like torque for FMR line-shape analysis. Pt was chosen as one of the most reliable materials with well-established parameters, especially in terms of θ_{SH}, crystal structure, and conductivity [15], while FeCoB has been shown to exhibit the highest tunneling magnetoresistance effect [16]

together with the MgO barrier [17]. It has been recently shown that creating additional interfaces [18], for example, by using Pt-Ti multilayer, θ_{SH} can be enhanced at the cost of the resistivity. Utilizing a simple two-step lithography procedure, the Hall-bar matrix of different thickness of Pt or Pt-Ti interface number was fabricated, which enables determination of the magnetization saturation, resistivity, magnetization damping, and spin Hall efficiency. Magnetotransport properties measurement protocol include both high-frequency dynamic characterization and low-frequency resistance and harmonic Hall voltage measurements characterized by an ultra-low noise. Investigation within the two frequency regimes allows us to determine all mentioned magnetotransport properties in a single device. For this, a multi-probe RF rotating probe station was designed, which is controlled by a linear driver, enabling detailed measurement with an nV resolution. Using the presented protocol, we investigate both Pt/FeCoB and Pt-Ti/FeCoB bilayer properties that are the most relevant for device applications.

II. Experiment

A. Deposition and Microlithography

Multilayer stacks were deposited using magnetron sputtering on thermally oxidized 4-in Si wafer, with a wedged-shaped Pt layer in a Singulus Timaris cluster tool system. The following structure with Pt: Ta(1)/Pt(t_{Pt})/$Fe_{60}Co_{20}B_{20}$(2)/Ta(2) (thickness in nm) with t_{Pt} varying from 4 to 16 nm and Pt-Ti: Ta(1)/[Pt(d)/Ti(0.2)]$_m$/Pt(d)/$Fe_{60}Co_{20}B_{20}$(2)/Ta(2), where $(m + 1) \times d = 6$ nm for $m = 3$, 5, and 7 interlayers, were deposited and annealed at 310 °C in ultra-high vacuum chamber. The annealing step is required for a crystallization of the CoFeB along with the MgO tunnel barrier of the magnetic tunnel junction for further applications. The slope of the Pt-wedge is 1.2 nm/cm. The top Ta layer oxidizes after exposing to the atmospheric condition, forming a protective layer, while the bottom Ta layer serves as a buffer. After the deposition process, the multilayers were patterned into 200 μm $\times$ 30 μm stripes for resistance measurements and 30 μm $\times$ 10 μm Hall-bars for static and dynamics transport characterization, using optical lithography, lift-off, and ion-beam etching processes. The long axis of the stripes is perpendicular to the wedge direction, resulting in a negligible variation of the Pt thickness in a single device. Ti(5)/Au(50) contact electrodes were fabricated in a second lithography step. Devices enable resistance measurement using the four-point method, harmonic Hall voltage measurements, and FMR using the so-called spin-diode effect [19].

B. Transport Measurement

The Hall voltage signal was measured using low-frequency (2387 Hz) stimuli of 1 V in both out-of-plane and in-plane magnetic field. Depending on the sample resistance, the current (current density) ranged from 2.2 to 10 mA (5.2–7.2 MA/cm^2). FMR was measured using amplitude-modulated RF signal of $P = 16$ dBm applied to the long axis of the stripe and measurement of the mixing voltage (V_{mix}) using short-axis electrodes with a lock-in amplifier synchronized with the modulating signal. Harmonic Hall voltage measurements were performed in a fixed magnetic field with a rotating sample stage with an RF-multiprobe from T-plus attached. The mechanical rotation of the stage was controlled with a stepper motor driven by the dedicated linear controller.

C. Rotating Probe Station

Detailed investigation of the spin Hall effect requires measurement in a magnetic field applied at various angles with respect to the Hall-bar axis. Specifically, anisotropy field H_k is determined from anomalous Hall effect (AHE) measured in a perpendicular magnetic field, while harmonic Hall voltage investigation requires rotation of the in-plane magnetic field vector. Dedicated mechanical setup was designed and fabricated by MeasLine Ltd., Skawina, Poland, which enabled rotation of the sample at an arbitrary polar and azimuth angle with respect to the magnetic field produced by the dipole electromagnet. To reduce the noise, a dedicated stepper driver controller was designed.

A standard stepper motor driver incorporates pulse width modulation (PWM) signal to tune and stabilize coil current of the motors. This current must be applied to the motor even when stationary, to hold the position while using microstepping (i.e., ability to move motor more precise than its full step resolution). While PWM signal allows to reduce size of the driver unit and increase its power efficiency, it also generates a switching noise. This causes generation of dynamic electromagnetic fields around the motors and cabling, which significantly disrupts precise measurements performed in the rotating setup due to radio frequency interference (RFI). The spectra of this interference are broad, as it originates from a square-shape PWM waveform. In order to eliminate it, a specialized driver was designed, which uses a linear (i.e., nonswitching) voltage sources for the motors with negligible RFI. Additionally, a dedicated printed circuit board was designed to minimize the electromagnetic interference from the board itself.

The stepper motor driver was built using multiple high-current digitally controlled voltage sources. Instead of using a PWM signal, digital to analog converters (DACs)—dual-channel 14-b AD5643R—provide a voltage corresponding to the requested motor's phase current. Operational amplifiers—OPA548T—uses 0–2.5-V voltage from DAC and convert it to bipolar $\pm$9 V. Each coil of the motor has its own DAC and the driver, in addition to the total of four drivers [Fig. 1(b)]. A 32-b ARM microcontroller STM32F103C8T6 is responsible for receiving commands from the measurement software using FT230XQ USB interface, creating trapezoidal motion profiles (to smoothly start and end the movement) and controlling DACs by generating required voltages for each motor phase. Maximum voltages per phase, parameters of trapezoidal motion profiles, and microstepping factors can be adjusted by sending configuration commands. Whole system is powered using an external linear laboratory power supply, which is also controlled by a designed unit. Additionally, the USB interface is completely opto-isolated from the system,

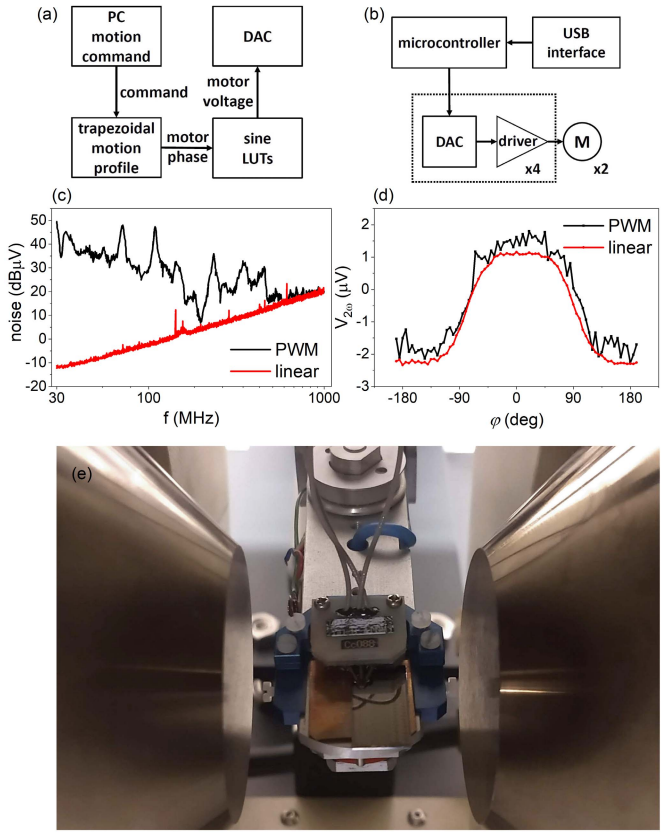

Fig. 1. Microwave rotating probe station design: (a) software flow, (b) driver's hardware block-diagram, (c) comparison of the switching and linear driver performance in terms of the electromagnetic radiation, and (d) second harmonic Hall measurements. (e) Photograph of the rotating probe station.

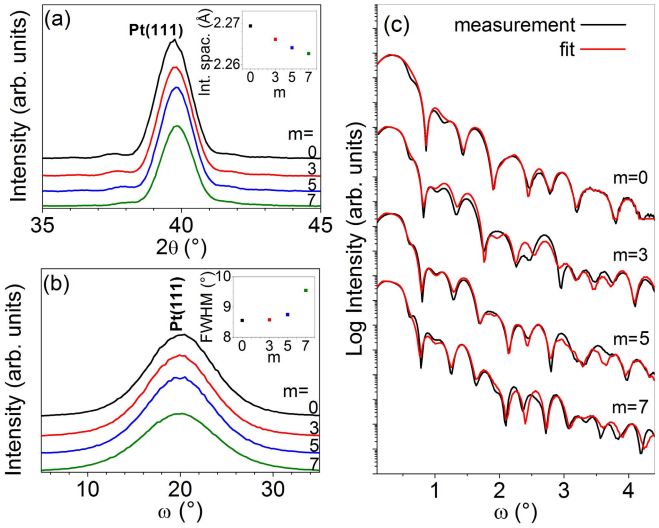

Fig. 2. X-ray diffraction (XRD) and X-ray reflectivity (XRR) measurements of the investigated multilayers. (a) Intensity of the Pt(111) peak decreases with increasing Ti interfaces. In addition, the peak position shifts to higher angles with higher m, which is interpreted as a decrease in interplanar distances of Pt (inset). (b) Rocking curves are resulting in an increase of FWHM with m (inset). (c) XRR for all multilayers together with corresponding fits. The fitting parameters are collected in Table I.

which protects the PC in the case of mains power issues. A software flow is shown in Fig. 1(a).

Fig. 1(c) presents the comparison of the measured radiation emissions correlated to 10-m open area test site (OATS) for both PWM (based on Leadshine EM402 driver) and the presented linear driver. Measurements were performed using a GHz transverse electromagnetic (GTEM) chamber, calculated and correlated according to electromagnetic interference standards [20]. To verify the operation of the driver, the angular measurement of the second harmonics Hall voltage dependence on the in-plane magnetic field was determined [Fig. 1(d)], which shows an improvement with respect to the PWM-based driver in terms of the measurement noise. An image of the entire probe station is presented in Fig. 1(e). Specifically, both in-plane and out-of-plane magnetic field characteristics as well as angular dependence using the four-point technique can be measured upon contacting the device under test, which is an advancement to the previously published setup [21], [22].

III. Results and Discussion

A. X-Ray Diffraction, Resistivity, and Anomalous Hall Effect

X-ray diffraction (XRD) patterns for both Pt- and Pt-Ti-based multilayers are presented in Fig. 2(a). The intensities of θ–2θ XRD peaks decrease together with increasing the number m of the Pt-Ti multilayers. The lattice plane spacing calculated from the position of Pt (111) decreases similarly to [14] (Fig. 2(a), inset). For both Pt- and Pt-Ti-based samples, the grain size in the direction perpendicular to the layers, calculated from the Scherrer equation, are comparable to the Pt and Pt-Ti thickness. Fig. 2(b) shows the XRD rocking curve patterns of Pt(111) for investigated structures. From fitting of the rocking curve peaks, a full-width at half-maximum (FWHM) parameter was determined [Fig. 2(b), inset]. The highest FWHM was calculated for the sample with the greatest number of Ti layers, which means that the Ti atoms diffused into Pt grains [23] after the deposition and annealing process. X-ray reflectivity (XRR) measurements and the corresponding fits for the Pt-Ti-based multilayers are shown in Fig. 2(c). Fitting parameters for samples with different number of Ti monolayers are collected in Table I. The fits were made by replacing the Pt-Ti superlattice with a single Pt layer with total $[\mathrm{Pt}(d)/\mathrm{Ti}(0.2)]_m/\mathrm{Pt}(d)$ thickness and reduced density (compared to the Pt density of 21.45 g/cm^3) as a result of dissolving Ti in Pt. This assumption was supported by a strong mixing enthalpy for Ti in Pt (−290 kJ/mole of atoms) and Pt in Ti (−290 kJ/mole of atoms) [24].

Around 100 devices with different t_{Pt} were used for resistivity (ρ) determination. For each device, the resistance (R) was transformed into sheet conductance $G_S = l/wR$, with l and w being the length and the width of the stripe, respectively. The resistivity of Pt was then calculated as $\rho_{\mathrm{Pt}} = t_{\mathrm{Pt}}/(G_S - G_0)$, where $G_0 = 0.0011$ S is the sheet conductance of the multilayer without Pt buffer. Similarly, the resistivity of the Pt-Ti $\rho_{\mathrm{Pt-Ti}}$ was calculated for different number of Pt-Ti interfaces. The results are presented in Fig. 3, together with a

TABLE I
XRR FITTING PARAMETERS—DENSITY (g/cm^3), THICKNESS (nm), ROUGHNESS (nm)—FOR Pt- AND Pt-Ti-BASED MULTILAYERS

	Pt			$[Pt\text{-}Ti]_3$			$[Pt\text{-}Ti]_5$			$[Pt\text{-}Ti]_7$		
	density	t	roughness	density	t	roughness	density	t	roughness	density	t	roughness
Si	2.33	-	0.27	2.33	-	0.26	2.32	-	0.31	2.33	-	0.26
SiO	2.64	100	0.31	2.64	100	0.29	2.64	100	0.34	2.64	100	0.26
Ta	16.6	1.10	0.46	13.3	0.86	0.24	14.1	0.99	0.21	13.6	0.98	0.35
Pt	21.4	5.97	0.47	16.9	6.69	0.44	17.4	7.05	0.48	17.0	7.44	0.43
FeCoB	8.13	1.89	0.36	8.31	1.88	0.42	8.29	1.87	0.37	8.38	1.76	0.44
Ta	15.9	0.36	0.50	13.3	1.36	0.36	13.5	1.26	0.34	13.0	1.35	0.36
Ta_2O_5	5.14	3.46	0.37	5.86	3.27	0.36	6.64	3.49	0.41	5.57	3.31	0.37

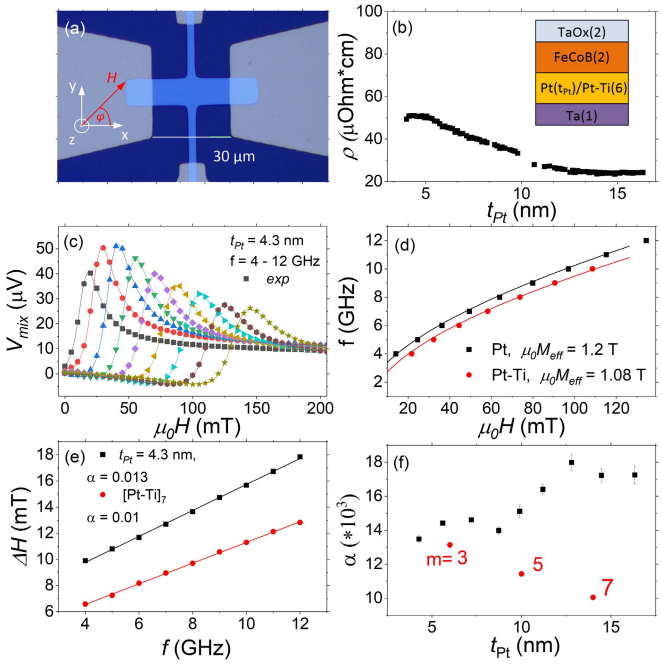

Fig. 3. (a) Micrograph of the Hall-bar, (b) resistivity versus Pt thickness dependence, (c) example of the FMR measured using spin-diode effect for different excitation frequency for the Hall-bar with $t_{Pt} = 4.3$ nm, (d) resonance frequency versus in-plane magnetic field for Pt ($t_{Pt} = 4.3$ nm) and Pt-Ti ($m = 7$) underlayers modeled using Kittel formula, (e) FMR linewidth (ΔH) versus frequency dependence, together with a line fit, enabling damping constant calculation, and (f) damping dependence on t_{Pt} and number of Pt-Ti interfaces.

micrograph of the Hall-bar. ρ_{Pt} versus t_{Pt} behavior resembles similar dependence measured in Pt/Co/MgO multilayers [25].

B. Saturation Magnetization and Damping

Saturation magnetization (M_S) for each underlayer was measured using a vibrating sample magnetometer, while the effective magnetization (M_{eff}) and magnetization damping (α) were determined from the FMR. To do so, the V_{mix} versus in-plane magnetic field (H) was measured for different input frequencies (f) spanning from 4 to 12 GHz. As a result, the family of Lorentz-shape curves were obtained, which were fitted using the formula

$$V_{mix} = V_S \frac{\Delta H^2}{\Delta H^2 + (H - H_0)^2} + V_{AS} \frac{\Delta H (H - H_0)}{\Delta H^2 + (H - H_0)^2} \quad (1)$$

where V_S and V_{AS} are the magnitude of symmetric and antisymmetric Lorentz curves, respectively, ΔH is the linewidth, and H_0 is the resonance field. f versus H_0 dependence was fitted using the Kittel formula [26], and the fitting parameters are presented in Table II. The dependence of damping on Pt thickness and Pt-Ti interfaces is depicted in Fig. 3(f). We note that for Pt-Ti buffer, the effective damping decreases with increasing number of interfaces (m), which may be useful for applications, as the critical current density needed to switch the ferromagnet depends linearly on the effective damping [27].

C. Spin Hall Angle

The spin Hall efficiency was determined from the harmonic Hall voltage measurements performed in the rotating in-plane magnetic field [28]. Fig. 4 presents angular dependence of the first (V_ω) and second ($V_{2\omega}$) harmonic Hall voltage versus azimuth angle φ between the magnetic field vector and long axis of the Hall-bar [as denoted in Fig. 4(a)]. Both dependencies were modeled using the following equation:

$$\begin{aligned} V_\omega &= V_P \sin 2\varphi \\ V_{2\omega} &= -\frac{V_P (H_{FL} + H_{Oe})}{H} \cos\varphi \cos 2\varphi \\ &\quad + -\left(\frac{V_A H_{DL}}{2H_{eff}} - V_{ANE} \right) \cos\varphi \end{aligned} \quad (2)$$

where V_P and V_A are the planar and anomalous Hall voltages, H_{FL}, H_{Oe}, and H_{DL} are the field-like, Oersted field, and damping-like field components, respectively, and $H_{eff} = H + H_k$ is the effective field, which is the sum of the external magnetic field and anisotropy field, determined from the AHE measurement in the perpendicular orientation (H along the z-axis). V_{ANE} is the additional contribution from the anomalous Nernst effect, which was found negligible in the investigated bilayers. The spin Hall efficiency ξ_{DL} was calculated using the formula

$$\xi_{DL} = \frac{\mu_0 M_S t_{FeCoB} H_{DL}}{j\hbar/2e}. \quad (3)$$

As a result of the calculation, the dependence of the spin Hall efficiencies was obtained as a function of t_{Pt}. Similar to [25] and [29], ξ_{DL} reaches its maximum for $t_{Pt} = 5$ nm and decreases with increasing thickness of HM. To account for the Oersted field, we used an analytical expression $H_{Oe} = J t_{Pt}/2$. The calculated values dominate the field-like contribution, which means that both H_{FL} and H_{Oe} are comparable in amplitude but of opposite sign. Nonetheless, ξ_{FL} is an order of magnitude smaller than ξ_{DL} for the thinnest Pt but increases with increasing t_{Pt}. The results of the effective field values

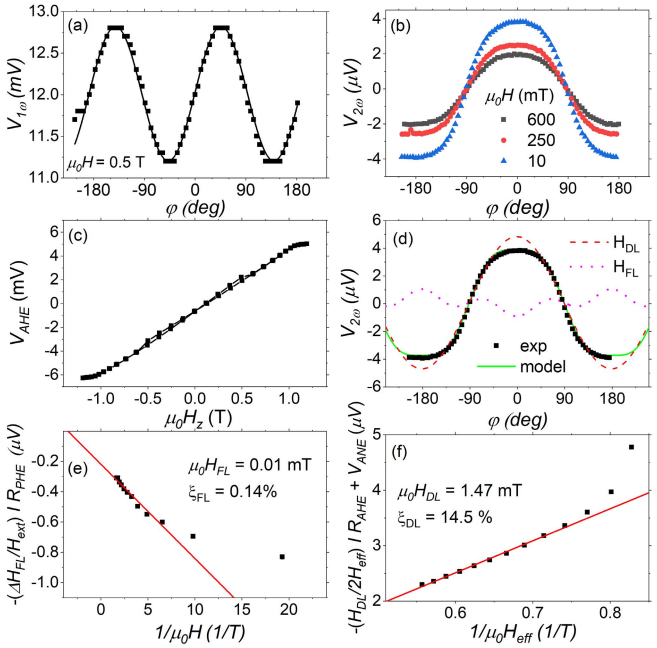

Fig. 4. Hall voltage measurements of the (a) first and (b) second harmonic components versus in-plane magnetic field angle of the Hall bar with t_{Pt} = 4.3 nm. (c) Anomalous Hall voltage measurement in the perpendicular field, that is, along *z*-axis enables anisotropy field determination. (d) Second harmonic Hall voltage was modeled using (2) enabling separation of the damping-like (H_{DL}) and field-like (H_{FL}) effective field components. (e) Dependence of the H_{FL} versus inverse of the applied magnetic field and (f) H_{DL} versus inverse of the effective magnetic field enables calculation of the spin Hall efficiencies.

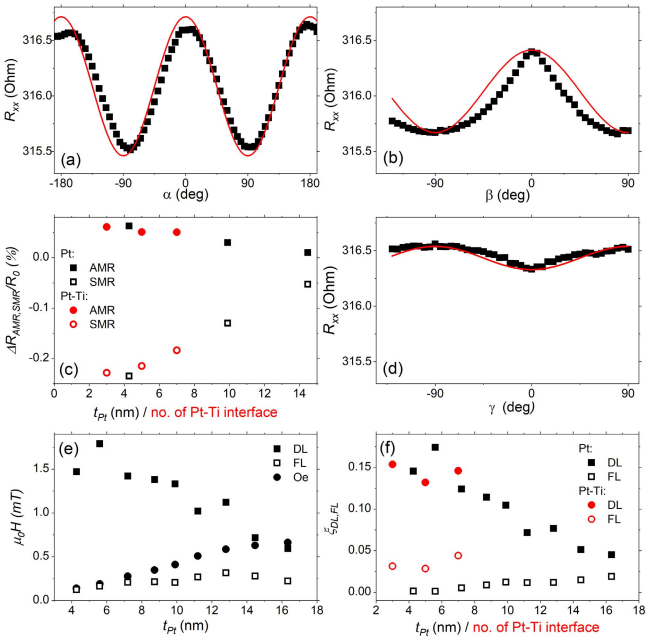

Fig. 5. (a)–(c) Example of the longitudinal resistance (R_{xx}) in different azimuth (α) and polar (β and γ) angles for t_{Pt} = 4.3 nm, enabling separation of the AMR and SMR contribution to the total magnetoresistance. (b) and (d) Measurements were performed in a magnetic field H = 1.8 T, which exceeds the anisotropy field, but is unable to saturate the FeCoB magnetization at polar angles $0 < \theta < 90$, hence a small deviation from the cosine dependence. (d) AMR and SMR values determined for different t_{Pt} and number of Pt-Ti interfaces. (e) Calculated effective fields in Pt-based elements. (f) As a result, the spin Hall efficiencies for all devices.

are presented in Fig. 5. In order to calculate the intrinsic θ_{SH}, one has to take into account the interface transparency. To do so, we first calculate the absorption of the spin current on the Pt/FeCoB interface using the following formula:

$$g_{\text{eff}}^{\uparrow\downarrow} = \frac{4\pi M_S t_{\text{FeCoB}}}{g\mu_B}(\alpha_{\text{eff}} - \alpha_0) \tag{4}$$

where g is the Lande factor, μ_B is the Bohr magneton, and $\alpha_0 = 0.004$ is intrinsic damping of FeCoB. $g_{\text{eff}}^{\uparrow\downarrow}$ for different Pt thickness and Pt-Ti underlayer were calculated and presented in Fig. 5. In general, $g_{\text{eff}}^{\uparrow\downarrow}$ increases (decreases) with the thickness of Pt (with a number of Pt-Ti interfaces) as a result of increasing (decreasing) damping constant. Next, the interface transparency T is calculated as

$$T = \frac{g_{\text{eff}}^{\uparrow\downarrow}\tanh\dfrac{t_{\text{Pt}}}{2\lambda_{\text{Pt}}}}{g_{\text{eff}}^{\uparrow\downarrow}\coth\dfrac{t_{\text{Pt}}}{\lambda_{\text{Pt}}} + \dfrac{h}{\rho_{\text{Pt}}\lambda_{\text{Pt}}2e^2}} \tag{5}$$

where $\lambda_{\text{Pt}} = 2$ nm is the spin diffusion length [30] in Pt, h is the Planck constant, and e is the electron charge. The calculated transparency, which varies slightly between 0.42 and 0.5 for Pt/FeCoB and Pt-Ti/FeCoB interfaces, were included in Table II. Finally, $\theta_{\text{SH}} = \xi_{\text{DL}}/T$ and spin Hall conductivity $\sigma_{\text{SH}} = \xi_{\text{SH}}/\rho_{\text{HM}}$ were calculated. We note that we took into account the transparency of the HM/FM interface to calculate the intrinsic spin Hall angle [15]. The spin Hall efficiency ranges between 0.17 and 0.05 depending on the thickness of Pt. Similar values were obtained using a line-shape analysis of the SOT-FMR signal, based on [31], SMR, and the current-assisted magnetic-field switching experiments [30]. Nevertheless, the intrinsic spin Hall angle is a function of the interface transparency determination, which depends on spin diffusion length and spin mixing conductance. In the presented analysis, the interface transparency ranges between 0.5 and 0.4, which results in θ_{SH} between 0.35 and 0.12. Smaller interface transparency would translate into even higher intrinsic θ_{SH}, which were recently reported in [14] and [32].

D. Magnetoresistance

To complete the spin-dependent transport analysis, the angular measurements of the magnetoresistance in x–y (α-rotation), y–z (β-rotation), and x–z (γ-rotation) planes were conducted [33]. Fig. 5 presents angular resistance dependence in Pt/FeCoB with $t_{\text{Pt}} = 4.3$ nm. Using the formulas from [34], SMR and anisotropic magnetoresistance (AMR) were derived [Fig. 5(c)]. The dependence of SMR on t_{Pt} and a number of Pt-Ti interfaces coincides with the dependence of the spin Hall conductivity, however, it does not match the dependence of the resistivity—for Pt underlayer, the highest SMR was determined in the bilayer with the thinnest Pt, whereas for Pt-Ti, the highest SMR was reported for the smallest number of Pt-Ti interfaces. The AMR contribution decreases with increasing t_{Pt} due to shunting effect from Pt [35].

TABLE II
SUMMARY OF THE SPIN TRANSPORT PARAMETERS DETERMINED IN PT-BASED (DIFFERENT THICKNESS) AND PT-TI-BASED (DIFFERENT NUMBER OF INTERFACES) DEVICES

t_{Pt}/	Pt			Pt-Ti			units
Pt-Ti intf.	5.6	10	14	3	5	7	nm/no.
ρ_{HM}	52	34	24	54	60	95	$\mu\Omega$cm
$\mu_0 M_S$	1.51	1.42	1.4	1.38	1.38	1.38	T
α	14	15	17	13	11	10	10^{-3}
$g_{eff}^{\uparrow\downarrow}$	16.3	16.8	19.6	13.4	10.4	8.9	10^{18}/m^2
T	0.5	0.46	0.42	0.48	0.44	0.51	
θ_{SH}	0.35	0.23	0.12	0.36	0.34	0.32	
σ_{SH}	3.3	3.07	2.13	3.2	2.6	1.75	$10^5/(\Omega m)$

There are a few materials reported with higher intrinsic spin Hall angle, including HMs: W [36], [37], Ta [9], and topological insulators: BiSe [38], however, at the cost of increased resistivity of the material. Similar tendency is maintained by alloying HMs with good conductors: AuPt [39] and AuTa [40]. Surprisingly, σ_{SH} for Pt reaches a maximum value of 3.3×10^5 S/m for 5.6-nm-thick underlayer, which is among one of the highest values reported for Pt [41]–[43], Pt-based multilayers [18] and alloys [44], exceeding other HM and their compounds [45], mainly due to small resistivity of the Pt. Even higher intrinsic spin Hall angle has been measured recently in an all-epitaxial ferrite/Pt system [32]. This finding, together with well-established deposition technique, crystal properties, and endurance, leads to the conclusion that Pt is one of the most optimal materials for SOT applications in line with potential spin-logic circuits [46].

IV. SUMMARY

In summary, the measurement protocol of the spin orbit torque efficiency based on low-frequency harmonic Hall voltage measurement and RF ferromagnetic resonance analysis was presented. The design of the setup including a rotating probe station and a dedicated linear driver together with microfabricated Hall bar bilayers based on FeCoB with different underlayer materials was shown, which enables a thorough analysis of the spin-dependent phenomena in HM/FM bilayer system. The protocol was verified in Pt- and Pt-Ti-based devices, resulting in an intrinsic spin Hall angle of up to 0.35 and spin Hall conductivity reaching 3.3×10^5 S/m, which is among the highest values reported. Our findings indicate that Pt remains one of the most attractive material for spintronics.

ACKNOWLEDGMENT

Nanofabrication was performed at the Academic Centre for Materials and Nanotechnology, AGH University of Science and Technology, Kraków, Poland.

REFERENCES

[1] A. Hirohata *et al.*, "Review on spintronics: Principles and device applications," *J. Magn. Magn. Mater.*, vol. 509, Sep. 2020, Art. no. 166711.
[2] R. Andrawis, A. Jaiswal, and K. Roy, "Design and comparative analysis of spintronic memories based on current and voltage driven switching," *IEEE Trans. Electron Devices*, vol. 65, no. 7, pp. 2682–2693, Jul. 2018.
[3] B. Dieny *et al.*, "Opportunities and challenges for spintronics in the microelectronics industry," *Nature Electron.*, vol. 3, no. 8, pp. 446–459, Aug. 2020.
[4] J. Grollier, D. Querlioz, and M. D. Stiles, "Spintronic nanodevices for bioinspired computing," *Proc. IEEE*, vol. 104, no. 10, pp. 2024–2039, Oct. 2016.
[5] J. E. Hirsch, "Spin Hall effect," *Phys. Rev. Lett*, vol. 83, no. 9, pp. 1834–1837, Aug. 1999.
[6] A. Hoffmann, "Spin Hall effects in metals," *IEEE Trans. Magn.*, vol. 49, no. 10, pp. 5172–5193, Oct. 2013.
[7] I. M. Miron *et al.*, "Perpendicular switching of a single ferromagnetic layer induced by in-plane current injection," *Nature*, vol. 476, no. 7359, pp. 189–193, Aug. 2011.
[8] L. Liu, C.-F. Pai, Y. Li, H. W. Tseng, D. C. Ralph, and R. A. Buhrman, "Spin-torque switching with the giant spin Hall effect of tantalum," *Science*, vol. 336, no. 6081, pp. 555–558, 2012.
[9] L. Liu, T. Moriyama, D. C. Ralph, and R. A. Buhrman, "Spin-torque ferromagnetic resonance induced by the spin Hall effect," *Phys. Rev. Lett.*, vol. 106, no. 3, 2011, Art. no. 036601.
[10] J. Kim *et al.*, "Layer thickness dependence of the current-induced effective field vector in Ta|CoFeB|MgO," *Nature Mater.*, vol. 12, pp. 240–245, Dec. 2013.
[11] C. Stamm *et al.*, "Magneto-optical detection of the spin Hall effect in Pt and W thin films," *Phys. Rev. Lett.*, vol. 119, no. 8, Aug. 2017, Art. no. 087203.
[12] H. Nakayama *et al.*, "Spin Hall magnetoresistance induced by a nonequilibrium proximity effect," *Phys. Rev. Lett.*, vol. 110, no. 20, May 2013, Art. no. 206601.
[13] Q. Hao and G. Xiao, "Giant spin Hall effect and switching induced by spin-transfer torque in a $W/Co_{40}Fe_{40}B_{20}/MgO$ structure with perpendicular magnetic anisotropy," *Phys. Rev. Appl.*, vol. 3, no. 3, Mar. 2015, Art. no. 034009.
[14] L. Zhu and R. A. Buhrman, "Maximizing spin-orbit-torque efficiency of Pt/Ti multilayers: Trade-off between intrinsic spin Hall conductivity and carrier lifetime," *Phys. Rev. Appl.*, vol. 12, no. 5, Nov. 2019, Art. no. 051002.
[15] G. D. H. Wong *et al.*, "Strain-mediated spin–orbit torque enhancement in Pt/Co on flexible substrate," *ACS Nano*, vol. 15, pp. 8319–8327, May 2021.
[16] S. Ikeda *et al.*, "Tunnel magnetoresistance of 604% at 300 K by suppression of Ta diffusion in CoFeB/MgO/CoFeB pseudo-spin-valves annealed at high temperature," *Appl. Phys. Lett.*, vol. 93, no. 8, 2008, Art. no. 082508.
[17] S. Yuasa, T. Nagahama, A. Fukushima, Y. Suzuki, and K. Ando, "Giant room-temperature magnetoresistance in single-crystal Fe/MgO/Fe magnetic tunnel junctions," *Nature Mater.*, vol. 3, no. 12, pp. 868–871, 2004.
[18] L. Zhu, D. C. Ralph, and R. A. Buhrman, "Spin-orbit torques in heavy-metal–ferromagnet bilayers with varying strengths of interfacial spin-orbit coupling," *Phys. Rev. Lett.*, vol. 122, no. 7, Feb. 2019, Art. no. 077201.
[19] A. A. Tulapurkar *et al.*, "Spin-torque diode effect in magnetic tunnel junctions," *Nature*, vol. 438, no. 7066, pp. 339–342, Nov. 2005.
[20] R. Guirado, R. del Rio, J. Carpio, F. Garnacho, A. Valladolid, and M. Valcarcel, "Comparison between GTEM and OATS radiated field emission measurements," in *Proc. Int. Symp. Electromagn. Compat.*, 1995, pp. 338–342.
[21] S. He, Z. Meng, L. Huang, L. K. Yap, T. Zhou, and C. Panagopoulos, "A versatile rotary-stage high frequency probe station for studying magnetic films and devices," *Rev. Sci. Instrum.*, vol. 87, no. 7, Jul. 2016, Art. no. 074704.
[22] S. Tamaru *et al.*, "Bias field angle dependence of the self-oscillation of spin torque oscillators having a perpendicularly magnetized free layer and in-plane magnetized reference layer," *Appl. Phys. Exp.*, vol. 7, no. 6, May 2014, Art. no. 063005.
[23] M. Kopcewicz, T. Stobiecki, M. Czapkiewicz, and A. Grabias, "Microstructure and magnetic properties of Fe/Ti multilayers," *J. Phys., Condens. Matter*, vol. 9, no. 1, pp. 103–115, Jan. 1997.
[24] F. D. Boer, W. C. M. Mattens, R. Boom, A. R. Miedema, and A. K. Niessen, *Cohesion in Metals*. Amsterdam, The Netherlands: North Holland, 1988.
[25] M.-H. Nguyen, D. C. Ralph, and R. A. Buhrman, "Spin torque study of the spin Hall conductivity and spin diffusion length in platinum thin films with varying resistivity," *Phys. Rev. Lett.*, vol. 116, no. 12, Mar. 2016, Art. no. 126601.
[26] C. Kittel, "On the theory of ferromagnetic resonance absorption," *Phys. Rev.*, vol. 73, no. 2, pp. 155–161, Jan. 1948.
[27] E. B. Myers, D. C. Ralph, J. A. Katine, R. N. Louie, and R. A. Buhrman, "Current-induced switching of domains in magnetic multilayer devices," *Science*, vol. 285, no. 5429, pp. 867–870, 1999.

[28] C. O. Avci *et al.*, "Interplay of spin-orbit torque and thermoelectric effects in ferromagnet/normal-metal bilayers," *Phys. Rev. B, Condens. Matter*, vol. 90, no. 22, Dec. 2014, Art. no. 224427.

[29] C. F. Pai, Y. Ou, H. L. Vilela-Leão, D. C. Ralph, and R. A. Buhrman, "Dependence of the efficiency of spin Hall torque on the transparency of Pt/ferromagnetic layer interfaces," *Phys. Rev. B, Condens. Matter*, vol. 92, no. 6, 2015, Art. no. 064426.

[30] A. Magni *et al.*, "Spin Hall magnetoresistance and spin orbit torque efficiency in Pt/FeCoB bilayers," *IEEE Trans. Magn.*, early access, May 28, 2021, doi: 10.1109/TMAG.2021.3084866.

[31] D. MacNeill, G. M. Stiehl, M. H. D. Guimaraes, R. A. Buhrman, J. Park, and D. C. Ralph, "Control of spin–orbit torques through crystal symmetry in WTe_2/ferromagnet bilayers," *Nature Phys.*, vol. 13, no. 3, pp. 300–305, Mar. 2017.

[32] P. Li *et al.*, "Charge-spin interconversion in epitaxial Pt probed by spin-orbit torques in a magnetic insulator," *Phys. Rev. Mater.*, vol. 5, no. 6, Jun. 2021, Art. no. 064404.

[33] S. Cho, S.-H. C. Baek, K.-D. Lee, Y. Jo, and B.-G. Park, "Large spin Hall magnetoresistance and its correlation to the spin-orbit torque in W/CoFeB/MgO structures," *Sci. Rep.*, vol. 5, Oct. 2015, Art. no. 14668.

[34] J. Kim, P. Sheng, S. Takahashi, S. Mitani, and M. Hayashi, "Spin Hall magnetoresistance in metallic bilayers," *Phys. Rev. Lett.*, vol. 116, Feb. 2016, Art. no. 097201.

[35] Ł. Karwacki *et al.*, "Optimization of spin Hall magnetoresistance in heavy-metal/ferromagnetic-metal bilayers," *Sci. Rep.*, vol. 10, no. 1, p. 10767, Jul. 2020.

[36] C.-F. Pai, L. Liu, Y. Li, H. W. Tseng, D. C. Ralph, and R. A. Buhrman, "Spin transfer torque devices utilizing the giant spin Hall effect of tungsten," *Appl. Phys. Lett.*, vol. 101, no. 12, 2012, Art. no. 122404.

[37] W. Skowroński *et al.*, "Temperature dependence of spin-orbit torques in W/CoFeB bilayers," *Appl. Phys. Lett.*, vol. 109, no. 6, 2016, Art. no. 062407.

[38] D. C. Mahendra *et al.*, "Room-temperature high spin–orbit torque due to quantum confinement in sputtered $Bi_xSe_{(1-x)}$ films," *Nature Mater.*, vol. 17, no. 9, pp. 800–807, Sep. 2018.

[39] L. Zhu, L. Zhu, S. Shi, D. C. Ralph, and R. A. Buhrman, "Energy-efficient ultrafast SOT-MRAMs based on low-resistivity spin Hall metal $Au_{0.25}Pt_{0.75}$," *Adv. Electron. Mater.*, vol. 6, no. 2, 2020, Art. no. 1901131.

[40] P. Laczkowski *et al.*, "Large enhancement of the spin Hall effect in Au by side-jump scattering on Ta impurities," *Phys. Rev. B, Condens. Matter*, vol. 96, no. 14, Oct. 2017, Art. no. 140405.

[41] W. S. Torres, J. F. Sierra, L. A. Benítez, F. Bonell, M. V. Costache, and S. O. Valenzuela, "Spin precession and spin Hall effect in monolayer graphene/Pt nanostructures," *2D Mater.*, vol. 4, no. 4, Sep. 2017, Art. no. 041008.

[42] W. Yan, E. Sagasta, M. Ribeiro, Y. Niimi, L. E. Hueso, and F. Casanova, "Large room temperature spin-to-charge conversion signals in a few-layer graphene/Pt lateral heterostructure," *Nature Commun.*, vol. 8, no. 1, p. 661, Sep. 2017.

[43] V. T. Pham *et al.*, "Ferromagnetic/nonmagnetic nanostructures for the electrical measurement of the spin Hall effect," *Nano Lett.*, vol. 16, pp. 6755–6760, Nov. 2016.

[44] L. Zhu, D. C. Ralph, and R. A. Buhrman, "Highly efficient spin-current generation by the spin Hall effect in $Au_{1-x}Pt_x$," *Phys. Rev. Appl.*, vol. 10, no. 3, Sep. 2018, Art. no. 031001.

[45] J.-Y. Kim *et al.*, "Enhancement of spin Hall conductivity in W–Ta alloy," *Appl. Phys. Lett.*, vol. 117, no. 14, Oct. 2020, Art. no. 142403.

[46] V. T. Pham *et al.*, "Spin–orbit magnetic state readout in scaled ferromagnetic/heavy metal nanostructures," *Nature Electron.*, vol. 3, no. 6, pp. 309–315, Jun. 2020.